Analysis of characteristic parameters of large-scale coronal waves observed by STEREO/EUVI

N. Muhr[1], A.M. Veronig[1], I.W. Kienreich[1], M. Temmer[1]

IGAM (Institute of Geophysics, Astrophysics and Meteorology), Institute of Physics, University of Graz, *Universitätsplatz 5, A–8010 Graz, Austria*

and

B. Vršnak[2]

Hvar Observatory, Faculty of Geodesy, University of Zagreb, *Kačićeva 26, HR–10000 Zagreb, Croatia*

nicole.muhr@uni-graz.at

Received _____; accepted _____

ABSTRACT

The kinematical evolution of four EUV waves, well observed by the Extreme UltraViolet Imager (EUVI) onboard the Solar-Terrestrial Relations Observatory (STEREO), is studied by visually tracking the wave fronts as well as by a semi-automatized perturbation profile method leading to results matching each other within the error limits. The derived mean velocities of the events under study lie in the range of 220–350 $\mathrm{km\,s^{-1}}$. The fastest of the events (May 19, 2007) reveals a significant deceleration of ≈ -190 m $\mathrm{s^{-2}}$ while the others are consistent with a constant velocity during the wave propagation. The evolution of the maximum intensity values reveals initial intensification by 20 up to 70%, and decays to original levels within 40–60 min, while the width at half maximum and full maximum of the perturbation profiles are broadening by a factor of $2-4$. The integral below the perturbation profile remains basically constant in two cases, while it shows a decrease by a factor of $3-4$ in the other two cases. From the peak perturbation amplitudes we estimate the corresponding magneto-sonic Mach numbers M_{ms} which are in the range of 1.08–1.21. The perturbation profiles reveal three distinct features behind the propagating wave fronts: coronal dimmings, stationary brightenings and rarefaction regions. All of them appear after the wave passage and are only slowly fading away. Our findings indicate that the events under study are weak shock fast-mode MHD waves initiated by the CME lateral expansion.

Subject headings: EUVI waves - perturbation profiles - corona - stationary brightenings

1. Introduction

Large-scale, large-amplitude disturbances propagating through the solar corona have been first observed by Moses et al. (1997) and Thompson et al. (1998) in images recorded by the Extreme Ultraviolet Imaging Telescope (EIT; Delaboudinière et al. 1995) onboard the Solar and Heliospheric Observatory (SoHO; Domingo et al. 1995), thereafter called 'EIT waves'. They were originally interpreted as the coronal counterparts of the chromospheric Moreton waves (Moreton & Ramsey 1960) as suggested by Uchida (1968) with his coronal fast-mode MHD wave interpretation of Moreton waves. Though this interpretation has been confirmed for several case studies (e.g. Thompson et al. 1999; Warmuth et al. 2001; Pohjolainen et al. 2001; Vršnak et al. 2002; Khan & Aurass 2002; Vršnak et al. 2006; Veronig et al. 2006; Muhr et al. 2010), the statistical characteristics of EUV and Moreton waves are quite different. In particular, EIT waves generally propagate at much lower velocities, $v \approx 200$–$400\ \mathrm{km\,s^{-1}}$, than Moreton waves, $v \approx 1000\ \mathrm{km\,s^{-1}}$ (e.g. Klassen et al. 2000; Biesecker et al. 2002; Thompson & Myers 2009). Thus, there is still an ongoing debate of whether EIT waves are really the coronal counterparts of Moreton waves. Additionally, it is still an open discussion whether they are caused by the flare explosive energy release or the erupting CME (e.g. Warmuth et al. 2001, 2004b; Zhukov & Auchère 2004; Cliver et al. 2005; Vršnak & Cliver 2008) and whether they are waves at all or rather propagating disturbances related to magnetic field line opening and restructuring associated with the CME liftoff (e.g. Delannée & Aulanier 1999; Chen et al. 2002; Attrill et al. 2007; Wills-Davey et al. 2007).

Numerical simulations of EIT waves as fast-mode magnetohydrodynamical (MHD) waves resulted in wave phenomena mimicking observational data quite closely (Wang 2000; Wu et al. 2001; Ofman & Thompson 2002; Ofman 2007). An interesting by-product of the simulations by Ofman & Thompson (2002) and Terradas & Ofman (2004) are stationary

brightenings in the vicinity of the launch sites, in line with observations of such areas at the fronts of EIT waves (Delannée & Aulanier 1999; Delannée 2000; Attrill et al. 2007). Delannée et al. (2007) suggested them to be a result of magnetic field restructuring during the CME liftoff generated either by Joule heating or an increase in density due to plasma compression. Simulations by Cohen et al. (2009) favored the latter interpretation with some additional effect due to increased temperature resulting from plasma compression.

Until the launch of the STEREO (Solar-Terrestrial Relations Observatory, Kaiser et al. 2008) mission in 2006, with the Extreme UltraViolet Imager (EUVI; Howard et al. 2008) onboard, observations of EIT waves were drastically limited by a ≈ 12 min cadence of the EIT instrument in the 195 Å passband. The identically built instruments EUVI-A and EUVI-B onboard the twin STEREO spacecraft observe the solar corona in four different EUV passbands with a high observing cadence (up to 75 s) and a large field-of-view (up to 1.7 $R_{\odot}$) from two different vantage points.

Studies of large-scale waves with STEREO/EUVI reveal velocities in the range of $\approx$ 200–400 $km\,s^{-1}$ and a decelerating character consistent with freely propagating large-amplitude MHD fast-mode waves (Veronig et al. 2008, 2010; Long et al. 2008; Kienreich et al. 2009). With simultaneous observations by the two STEREO spacecraft, it was for the first time possible to analyze the 3D nature of EIT waves with stereoscopic techniques (Kienreich et al. 2009; Patsourakos & Vourlidas 2009; Patsourakos et al. 2009; Ma et al. 2009; Temmer et al. 2011). Veronig et al. (2008), Long et al. (2008) and Gopalswamy et al. (2009) reported the refraction and reflection of a wave at the border of a coronal hole providing strong evidence for the wave nature of the phenomenon. However, Attrill (2010) questioned these findings, favoring instead the hypothesis of two simultaneously launched waves from two distinctively separated sites. In the EUVI wave event of 2010 January 17, studied by Veronig et al. (2010), first observations of the full 3D

wave dome and its lateral and radial expansion could be performed. In a recent study that became available during the revision process of the present paper, Long et al. (2011) analyze the kinematical aspects and the evolution of the full width at half maximum (FWHM) and integral of the 2007 May 19 and 2009 February 13 events with similar methods. Therefore we will discuss and compare their findings with our results in section 5. For recent reviews regarding the kinematics of large-scale EUV waves, their morphology and relationship to associated solar phenomena we refer to Wills-Davey & Attrill (2010) and Gallagher & Long (2010).

In this paper, we study high-cadence EUV observations of four well defined EUV waves observed by STEREO/EUVI that occurred between May 2007 and April 2010. These waves are special due to their pronounced amplitudes although they occurred during the extreme current solar minimum. Our study has the following main aims:

1. We apply and compare two different methods to derive the wave kinematics: visual tracking of the foremost part of wave front and a method based on the intensity profiles of the propagating perturbation.

2. Based on the perturbation profiles, we derive quantities which provide insight into the physical character of the phenomenon in terms of Mach numbers as well as evolution of the amplitude, width and integrated intensity of the disturbances.

3. The perturbation profiles are further studied with respect to associated phenomena, such as stationary brightenings, coronal dimmings and rarefaction regions behind the wave fronts.

2. Data and Observations

The four large-scale coronal waves under study were recorded by EUVI on 2007 May 19, 2009 February 13, 2010 January 17, and 2010 April 29. The EUVI instruments are part of the Sun Earth Connection Coronal and Heliospheric Investigation (SECCHI; Howard et al. 2008) instrument suite on board the STEREO-A (Ahead; ST-A) and STEREO-B (Behind; ST-B) spacecraft. The separation angle between ST-A and ST-B steadily increases by ≈45° per year. EUVI observes the chromosphere and low corona in four spectral passbands (He II 304 Å: T∼ 0.07 MK; Fe IX 171 Å: T∼ 1 MK; Fe XII 195 Å: T∼ 1.5 MK; Fe XV 284 Å: T∼ 2.25 MK) out to 1.7 $R_\odot$ with a pixel-limited spatial resolution of $1''.6$ pixel^{-1} (Wuelser et al. 2004). For the kinematical analysis we used all passbands if possible, while for the perturbation profiles only the 195 Å images were studied, where the wave signal is most prominent.

The EUVI wave event of 2007 May 19 was recorded by both STEREO spacecrafts (ST-A and ST-B) and was observable from the Earth view. High-cadence EUVI images in the 171 Å (75 s), 195 Å (600 sec), 284 Å (300 s) and 304 Å (300 sec) channels are available. This event was the first distinct EUV wave observed by EUVI, and was already studied in quite some detail by several authors (Long et al. 2008; Veronig et al. 2008; Gopalswamy et al. 2009; Kerdraon et al. 2010; Long et al. 2011) revealing a propagation velocity decelerating from ≈ 450 to 200 km s^{-1} as well as an associated type II burst indicating shock formation in the corona.

The event of 2009 February 13 was observed by both STEREO spacecraft, and occurred in perfect quadrature (separation angle of ≈ 90°). The wave was observed on disk in ST-B and on the limb in ST-A. These observations provided a unique basis to study the 3D nature of the wave. Patsourakos & Vourlidas (2009) and Kienreich et al. (2009) determined a propagation height of the wave of ≈ 100 Mm, with a mean (on-disk) velocity

of ≈ 230 km s^{-1}. For the analysis, 171 Å and 195 Å filtergrams of ST-B are available with a cadence of 300 s and 600 s, respectively.

On 2010 January 17, ST-A and ST-B were 134° apart from each other. The wave was observed in the eastern hemisphere of ST-B, which was situated 70° behind Earth on its orbit around the Sun. This event was unique due to the full 3D wave dome structure that was observed in the different EUVI channels with a lateral (on-disk) propagation velocity of ≈ 300 km s^{-1} and an upward propagation velocity of ≈ 600 km s^{-1} (Veronig et al. 2010). The EUVI-B imaging cadence is 2.5 minutes in the 171 Å, 5 minutes in the 195 Å, 2.5−5 minutes in the 284 Å, and 5 minutes in the 304 Å passband.

The event of 2010 April 29 was the last and strongest of four homologous waves observed by ST-B within a period of 8 hours at a position angle of 70° behind solar limb as seen from Earth (Kienreich et al. 2011). EUVI images in all four wavelengths are available during the event. However, the cadence of two hours in the 171 Å and 284 Å channels limited a possible wave tracking to the 195 Å and 304 Å channels. Due to a lack of wave signatures in the 304 Å channel, only 195 Å filtergrams with a cadence of 300 s are used for the analysis.

All EUVI filtergrams were reduced using the SECCHI_PREP routines available within SolarSoft. Furthermore, we differentially rotated each data set to a common reference time. In order to enhance faint coronal wave signatures, we derived running ratio (RR) images dividing each image by a frame taken 10 minutes earlier, as well as base-ratio (BR) images dividing each image by the last pre-event image. Finally, a median filter was applied to the images to remove small scale variations. RR images are used for the visual tracking of the coronal waves, since in RR images the signal of propagating disturbances is highest. The perturbation profiles are calculated from BR images, which provide better insight into the changes of physical parameters due to the passing wave front.

3. Analysis

The kinematical analysis of large-scale propagating disturbances is usually based on visual tracking of the outer edge of the wave front. Thus, the results are severely influenced by the observer and his/her interpretation of the wave front. Therefore, more objective and reproducible as well as automated methods are desirable. Two alternative semi-automated methods have been applied so far to study EUV waves: the Huygens plotting method (Wills-Davey & Thompson 1999) and the perturbation profile method (Warmuth et al. 2004a; Podladchikova & Berghmans 2005; Muhr et al. 2010; Veronig et al. 2010).

In this study we focus on the perturbation profile method because of several reasons. First, this semi-automated method provides insight into important physical parameters of the EUVI wave (amplitude, widths, Mach number). Second, it provides a semi-automated alternative to the reconstruction of the wave kinematics by visual tracking. Third, detailed analysis of the perturbation profiles provide information on associated phenomena not observable by eye, which can give us important insight into the underlying physics of the events. In the following, we describe the two different methods, i.e. the visual tracking method and perturbation profiles, and their application to the study of EUV waves.

3.1. Kinematics via visual tracking

We visually tracked the wave fronts in series of EUVI RR images. The eruption center was derived by applying circular fits to the earliest observed EUVI wave fronts on the 3D solar surface appearing as ellipses in the 2D projected image (Veronig et al. 2006). In order to enhance the statistical significance and to ensure a realistic error estimate for the wave center position, all available passbands were used to determine a mean value and standard deviation. For each event, we focussed for both, the visual and the perturbation profile

method, on the same specific 45° propagation sector, in which the disturbance is most pronounced. The chosen sectors are restricted by two great circles (parts of them are shown by black curves in Figures 1–4), which pass through the determined wave center. To obtain the wave kinematics, we calculated for each point of the wave front within the selected propagation sector its distance from the eruption center along great circles on the solar surface, and then averaged over them.

3.2. Kinematics by perturbation profiles

The second approach to analyze the EUV wave propagation is based on the perturbation profiles. The method starts at the eruption center determined from the visually tracked wave fronts (see section 3.1) and sums the intensity values of all pixels between two constantly growing concentric circles (again in the deprojected heliospheric plane) defining annuli with a radial width of 1° within the selected propagation sector, which span over an angular width of 45° (for an illustration see movie 1 of the online version). Due to the fact that the area over which we sum up the pixel values is steadily growing by moving to greater radii, each annulus is averaged over its pixel sum. This is resulting in a mean intensity as a function of distance measured along the solar surface from the wave center. The procedure is repeated for each frame, i.e. time step, until the EUV wave fades away.

In perturbation profiles, propagating disturbances can be identified as a distinct bump above the background level (intensity level of 1.0 in base ratio images). Modified Gaussian envelopes emphasizing the leading part of the wave bump are then fitted to the perturbation profiles for two reasons. First of all, perturbation profiles show roughly a Gaussian form (Wills-Davey 2006; Veronig et al. 2010; Kienreich et al. 2011) and secondly it is very useful for the robustness and automatization of the latter part of the profile algorithm, in which the positions of the leading edges of the waves are extracted. Downs et al. (2011) state that

the peak intensity may be strongly affected by the emission of CME material, whereas the foremost front corresponds to the actual wave. The trailing edge of the wave is also strongly influenced by features like stationary brightenings, flare emission, CME and dimming regions behind the wave front. Therefore we use modified Gaussian envelopes to the original data set. First of all, the original data is examined for the peak intensity. Then a simple Gaussian fit is applied to the first half of the wave bump from the maximum until the leading edge. Finally, the Gaussian envelope is mirrored at the position of the maximum. The result is a Gaussian fit matching the foremost leading edge of the wave fronts much better than simple Gaussian fits while for the rest of the wave bump a characteristic envelope shape is formed.

From the modified Gaussian fits to the perturbation profiles we derive the position of the wave front. Starting at the maximum amplitude level of each wave bump we define the leading edge of the wave fronts at the position where the Gaussian envelope to the profile falls below an intensity level of $I/I_0 = 1.02$, with I the intensity entries of the current image and I_0 the intensity entries of the base image. This value is reasonable due to the fact that the human eye is able to identify intensity changes of as small as 1–2% above the background level. Thus, this should provide us with a good measure when comparing the wave front positions from the perturbation profiles and the visual tracking.

3.3. Calculation of perturbation profile parameters

It is possible to gain useful information on the wave characteristics by extracting distinct wave parameters from the perturbation profiles. We derived the amplitude, the FW, the FWHM and the integral below the perturbation profile (down to the intensity ratio of 1.02). The FW of the wave is defined as the width of the Gaussian envelope, whereas the FWHM is defined as the distance between those two points where the intensity

level drops below 50% of the maximum value. The integral of the perturbation profiles is the area below the Gaussian fits.

The calculation of the magnetosonic Mach numbers is based on the peak perturbation amplitude values, $A_{\max}$, of each wave event, derived from the peak of the Gaussian fits to the profiles. Due to the definition of base ratio images, we know that an increase in the perturbation amplitude above the background level can be interpreted as $A = I/I_0$, where the intensity I in an optically thin coronal spectral line is given as

$$I = \int_h f(T, n_e) n_e^2 dh \,, \tag{1}$$

with the emission measure $EM = \int_h n_e^2 dh$ along the line of sight and the contribution function $f(T, n_e)$ depending on plasma temperature T and electron density n_e (Phillips et al. 2008). To obtain an intensity value in a relative broad EUV passband, like the EUVI 195 Å passband, the integral over several spectral lines has to be conducted. Since there is a temperature and density dependence for each spectral line, the following approximations are made: First, the integration is only along the pressure scale height H with an average constant density n (Wills-Davey 2006). Thus the intensity turns into $I \approx f(T, n_e) n_e^2 H$, with $n_e^2 H$ the emission measure EM. Second, the quiet Sun in the 195 Å passband is dominated by its strongest line at 195.12 Å (Del Zanna et al. 2003) which is formed in a narrow temperature range of 1.2 MK to 1.8 MK, with the peak response at $\approx$ 1.4 MK (Feldman et al. 1999). In Fig. 3 of Zhukov (2011) it is evident that the contribution function of the 195.12 Å spectral line only weakly depends on density, i.e. $f(T, n_e) \approx f(T)$, and only weakly depends on temperature near its peak response which is also the position where the differential emission measure peaks. Thus and under the assumption that the temperature does not change considerably by the passing wave front, the relative intensity change I/I_0 (with I and I_0 referring to the initial and final state, respectively) can be used to estimate the density increase $n/n_0 \sim (I/I_0)^{1/2}$. Zhukov (2011) gives a detailed discussion of this

approach under consideration of the usage of the CHIANTI atomic database.

For each wave we estimate the density jump $X_c = n/n_0$ at the peak amplitude of the perturbation profile. Assuming the shock height to be in the low solar corona (Veronig et al. 2010), we can conclude from typical EUV wave velocities in the range of $200-500\ \mathrm{km\,s^{-1}}$ that the assumption of a quasi-perpendicular fast-mode MHD shock is reasonable (Mann et al. 1999). Considering the Rankine-Hugoniot jump conditions at a perpendicular shock front (e.g., Priest 1982), the magnetosonic Mach number $M_{ms} = v_c/v_{ms}$ (where v_c is the coronal shock velocity and v_{ms} the magnetosonic speed) can be expressed as

$$M_{ms} = \sqrt{\frac{X_c(X_c + 5 + 5\beta_c)}{(4 - X_c)(2 + 5\beta_c/3)}}\,, \tag{2}$$

where β_c is the ambient coronal plasma-to-magnetic pressure ratio, $X_c = n/n_0$ is the density jump at the shock front, and for the specific-heat ratio (the polytropic index) we substituted $\gamma = 5/3$. For the plasma beta in the quiet Sun we assume a value of $\beta_c = 0.1$ and note that Eq. 2 depends only weakly on β (Vršnak et al. 2002).

3.4. Coronal dimmings, stationary brightenings and rarefaction regions

Beside the propagating bright coronal wave front, the perturbation profiles show some other distinct features characterized either through persistent intensity depression (coronal dimmings and rarefaction regions) or intensity enhancement (stationary brightenings).

Coronal dimmings are regions of dramatically decreased plasma density occurring after the CME lift-off. They are usually interpreted as plasma evacuation due to the field line opening during the CME eruption (Hudson et al. 1996; Harra & Sterling 2001; Harra et al. 2007), and may last for several hours up to a day. We stress that there are different types of coronal dimmings, those in the near vicinity of the eruption site, referred to as core coronal dimmings, and so-called secondary dimmings further away from the eruption

site (Mandrini et al. 2007; Muhr et al. 2010). In this paper we deal with core coronal dimmings. They usually consist of two areas marking the footpoints of the erupting flux rope (Mandrini et al. 2005; Crooker & Webb 2006; Muhr et al. 2010) and show an intensity decrease of $\approx$ 40–60 % (e.g. Chertok & Grechnev 2005).

Stationary brightenings form at the edge of core coronal dimmmings and are noticed as intensity enhancements (e.g. Cohen et al. 2009). They are formed after the wave passage and last for a period of several tens of minutes until fading away. A possible explanation for their formation is that they are a result of material flow, storage and compression at this specific location due to an obstacle that can not be overcome easily (Delannée & Aulanier 1999; Delannée et al. 2007).

Rarefaction regions are expected to occur right behind a propagating wave pulse, clearly visible by an intensity amplitude below the background intensity (Landau & Lifshitz 1987). The moving wave pulse is a region of compressed plasma, continuously compressing the plasma in front of itself. Consequently, in the section behind the wave pulse a rarefaction region is formed, expanding to a certain distance. The wave travels at a velocity higher than the surrounding Alfvén velocity and thus the region behind the pulse is thinned out. The pressure and density in this region falls below the equilibrium values. The rarefaction region is the result of this evacuation due to the wave propagation. In contrast to the coronal dimming, which may be stationary and in most cases relatively huge, the rarefaction region propagates following the wave pulse and can be noticed as a small, localized dip in the rear section of the perturbation profile between the wave pulse and the coronal dimming.

4. Results

4.1. Wave kinematics

In Figures 1–4, the morphology and evolution of the four EUVI wave events under study is shown in BR images. We note that the wave fronts are not observed in the near vicinity of the eruption center but are first visible at distances of ≈ 240 Mm, 90 Mm, 150 Mm and 260 Mm from the respective initiation centers of 2007 May 19, 2009 February 13, 2010 January 17, 2010 April 29 event and can be followed up to distances of 600–900 Mm.

The top panels of Figures 5–8 show the distance-time plots of the events. We display the wave kinematics derived from both methods (visually tracking and perturbation profiles) together with error bars, linear and quadratic least square fits to the visually tracked wavefronts, as well as 95% confidence intervals and prediction boundaries of the linear fits. The mean velocities derived for the four events under study lie in the range of 220–350 $\mathrm{km\,s^{-1}}$.

Three of the four events propagate with constant speed. The small deceleration values derived from the quadratic fits are in the range of -6 to -13 $\mathrm{m\ s^{-2}}$, which corresponds to a deceleration of ≈ 5% with respect to the start velocity values derived from the quadratic fit to the wave kinematics. This lies within the confidence intervals, and thus it is justified to represent the kinematics of the three events by a propagation with constant velocity over the full propagation distance. We note that the kinematical analysis of the perturbation profiles of these three events reveal a somewhat stronger deceleration as compared to the visual tracking method, but they are still only marginally significant corresponding to a deceleration rate of ≈ 10% of the start velocity values. Only for the 2007 May 19 event, we obtain a significant deceleration of -193 $\mathrm{m\ s^{-2}}$, which corresponds to 30% of the start velocity. This is also the fastest wave in our sample with a mean velocity of

$\approx 350\ \mathrm{km\,s^{-1}}$. In Table 4.1, the derived information on the propagation characteristics (velocity, deceleration) are summarized.

Event	S/C	v_{lin} [km s^{-1}]		$v_{quad,0}$ [km s^{-1}]		a_0 [m s^{-2}]		I_{max}	X_c	M_{ms}
		vis.	prof.	vis.	prof.	vis.	prof.			
2007 May 19	ST-A	348±29	338±18	483±73	429±58	-193.2 ± 87	-84.7 ± 60	1.61	1.27	1.21
2009 Feb 13	ST-B	228±17	221±36	237±72	261±72	-6.9 ± 25	-23.4 ± 30	1.39	1.18	1.14
2010 Jan 17	ST-B	286±7	275±17	300±24	314±53	-13.4 ± 38	-39.4 ± 49	1.59	1.26	1.20
2010 Apr 29	ST-B	337±27	321±23	342±88	361±76	-7.6 ± 52	-51.7 ± 93	1.22	1.12	1.08

Table 1: EUVI wave properties of the events under study. We list the mean velocity values v_{lin} derived from linear fits, as well as the start velocity values $v_{quad,0}$ and the acceleration values a_0 derived from the quadratic fits for both methods, i.e. visual tracking method and profile method. Additionally, the peak intensity-amplitudes extracted from the perturbation profiles together with the density jump values X_c and the calculated Mach numbers M_{ms} are listed.

We note that the position measurements of both methods match each other quite well, the maximum differences lie within an average of 20–40 Mm. As a consequence, also the velocity values derived via visual tracking correspond to these obtained by the perturbation profiles, and both values agree within the error limits (see Table 4.1).

4.2. Overall characteristics of perturbation profiles

The consistent kinematical results obtained with both methods suggest the perturbation profile method to be an adequate alternative to the visual tracking method. In particular, it is an additional possibility to analyze large-scale disturbances in the solar atmosphere by producing kinematical results not burdened by subjective judgements of the observer. Thus, the perturbation-profile results are easier to reproduce than those derived by the visual-tracking method.

Moreover, we can quantify various important wave parameters from the perturbation profiles. Figures 9 – 12 show for the four wave events under study the evolution of the perturbation profiles. In all four cases we observe a clear intensification in their early phase reaching its peak amplitude $A_{\max}$ value around 10 – 20 minutes (second or third panel of Figures 9 – 12) after the first remarkable wave bump can be observed. The evolution of the intensity amplitudes of all events under study is displayed in the middle panels of Figures 5–8. The peak perturbation amplitudes $A_{\max}$ lie in the range of 1.2−1.6. The calculated density jump values, X_c, are therefore in the range of 1.1−1.3, and the peak magnetosonic Mach numbers, M_{ms}, lie in the range of 1.08−1.21 (Table 4.1).

In addition, we derived the full width of the wave as well as the FWHM. The evolution of the pulse width is plotted in the bottom panel of Figures 5 – 8 for the four wave events under study. The width of the wave pulse as well as the FWHM increases during its evolution by a factor of 2–3, whereas the integral below the perturbation profile remains basically constant for the events of 2007 May 19 and 2010 April 29, and decreases for the events of 2009 February 13 and 2010 January 17 by a factor of 4 and 3, respectively.

4.3. Distinct features observable in the perturbation profiles after the wave passage

The inspection of the derived BR perturbation profiles reveals a diversity of distinct features after the wave passage, including coronal dimmings, stationary brightenings, and rarefaction regions. In the following, these are discussed individually for each of the four events in our sample.

4.3.1. Event of 2007 May 19

The profiles of 2007 May 19 show three distinct phases: the leading wave pulse (enveloped by gaussian fits), a reversal point (where the intensity level switches from values greater than 1.0 to below 1.0) and the trailing rarefaction region. Additionally, in the rear section of the perturbation profiles we observe a deep core dimming extending from the initiation site up to $\approx$ 300 Mm, with an intensity decrease of $\approx$ 70% lasting for several hours (Fig. 9).

The rarefaction region and its propagation is of special interest. This phenomenon is theoretically predicted to be located behind the propagating front of a compression wave but observations are barely reported (Cohen et al. 2009). From 12:52 UT until 13:02 UT we observe the formation of a deep coronal dimming behind the wave pulse. During its early evolution it becomes more pronounced and reaches its maximal spatial extension at 13:02 UT. After 13:02 UT it is quasi stationary. However in the frontal part of the dimming, from 300 Mm up to the trailing part of the wave pulse, a smaller, propagating dip is clearly visible. We interpret this as the rarefaction region following the wave front. Its formation is a combination of two aspects: 1) the driver stops at a distance of $\approx$ 300 Mm (where the outermost point of the deep-dimming region is located), and 2) behind the wave pulse the wave forms a region where the density and pressure fall below the equilibrium level.

This event was associated with a metric type II burst, indicating shock formation in the corona. We use the observations of the type II burst to obtain an alternative estimate of the shock Mach number. Type II bursts usually show the fundamental and harmonic emission band, both frequently being split in two parallel lanes, so-called band-split (Nelson & Melrose 1985). The interpretation of the band split as the plasma emission from the upstream and downstream shock regions was affirmed by Vršnak et al. (2001). Thus, the band-split can be used to obtain an estimation on the density jump at the shock front

and thus the Mach number of the ambient plasma (Vršnak et al. 2002).

The composite dynamic radio spectrum (Fig. 13) shows complex and intense radio emission, consisting of a group of type III bursts and a type II burst. For a detailed dynamic spectrum analysis covering the frequency range 0.4 – 300 MHz, we refer to Fig. 4 in Kerdraon et al. (2010). In the present study we focus on the type II burst that started around 12:51:30 UT at a frequency of 160 MHz. In the period 12:51:30 UT to 12:54:00 UT we were able to recognize a band-split pattern (indicated in Fig. 13 as two black lines), with a relative bandwidth of $BDW = \Delta f/f \approx 0.19 - 0.22$. The relative bandwidth BDW is determined by the density jump at the coronal shock front $X_c = \rho_{2c}/\rho_{1c}$, where ρ_{1c} and ρ_{2c} are the densities upstream and downstream of the shock front (for details see Vršnak et al. 2001). Since BDW$\equiv (f_2 - f_1)/f_1 = \sqrt{(\rho_{2c}/\rho_{1c})} - 1$, we find $X_c = 1.41 - 1.48$. Using a 5-fold Saito coronal density model (Saito 1970), we find from the derived values of the density jump X_c a Mach number of 1.32 – 1.40.

From the peak amplitude of the EUVI perturbation profile we derived $M_{ms} \approx 1.21$. A possible explanation for the smaller estimate is that, due to the width of 45° over which the perturbation profiles were derived, eventual higher values are averaged out (see Figure 9). The curve displayed by small black crosses shows the overall 45° sector we used for our analysis, while the grey line profile is displaying a small 2° sub-sector in the central part of the overall 45° sector. By shrinking the sector to a narrower width around the most intense propagation direction, we obtain a considerably higher peak due to a lower signal averaging, and the Mach number is increased to values of at least $M_{ms} = 1.3$. We note that the sector narrowing and the subsequent increased Mach number implies that the extracted values are (in fact always) underestimated and thus a lower limit for the Mach number estimate. Comparing the results of both approaches we find the Mach number of the ambient plasma to be $M_{ms} = 1.2 - 1.4$, a reasonable range of values for a coronal shock wave (Vršnak et al.

2001). Since EUV waves and type II bursts are generated at different heights in the solar atmosphere the Mach numbers are not necessarily the same. In particular, type II bursts are point-like sources formed where the disturbance is most intense, corresponding to higher Mach numbers. Shocks having Mach numbers in the range of 1.2–1.4 as determined for the events under study are usually considered as weak shocks.

4.3.2. Event of 2010 January 17

The perturbation profiles of 2010 January 17 show persistent stationary brightenings (Figures 10). They appear after the wave front passage and are only slowly fading away (Delannée & Aulanier 1999; Attrill et al. 2007; Delannée et al. 2007). The EUV wave starts at 03:56 UT as a relatively small wave pulse that is intensifying until 04:01 UT. In the subsequent panels of Figure 10, after the wave has intensified up to its maximum amplitude of 1.6 at 04:01 UT, a strong and long-lasting, quasi-stationary bright feature becomes clearly visible. We find first evidence for this stationary parts at 04:06 UT at a distance of 100–300 Mm from the source location, i.e. at the distance of the first wave front appearance (see Figure 10). It is well pronounced and exceeds an amplitude level of 1.25, lasting for at least 30 min after the wave passage. Compared to the time scale of the propagating disturbance it is only slowly fading away. This evolution can also be seen in the BR images in Figure 3, where we overplotted the position of the stationary brightenings by grey lines.

4.3.3. Event of 2009 February 13

The perturbation profiles of the quadrature event of 2009 February 13 are shown in Figure 11. The evolution of the most enhanced direction of 45±22.5° is displayed in the perturbation profiles by crosses. The propagating wave pulse can be clearly identified.

The grey line profile represents a different sector with its main direction to be 270±22.5°. It is characterized by an intensity enhancement which can be interpreted as a stationary brightening, showing a similar evolution like the one of 2010 January 17. The maximum intensity of these stationary brightenings is even more pronounced than that of the 2010 January 17 event and exceeds a level of 1.35 at 05:55 UT at 100–300 Mm from the source location (see Figure 11). It is again induced by the wave front passage and only slowly fading away. The propagating wave pulse ahead of the stationary brightening is not as pronounced as for the main direction but still detectable although it is considerably smaller than the stationary brightening. In both directions the coronal dimming is clearly visible. Its location is restricted to the area behind the stationary brightening at a distance up to ≈ 100 Mm.

4.3.4. Event of 2010 April 29

The wave event of 2010 April 29 is the fourth and strongest of four homologous waves that occurred within a time range of 8 hours (Kienreich et al. 2011). The profile evolution of the event is displayed in Figure 12. We can identify three different parts in the rear section of this perturbation profile: a dimming region, a stationary brightening and a rarefaction region, all visible after the waves' passage. The dimming region is prominent from the first image at 06:20 UT until the last profile shown at 06:40 UT, occurring at 0–100 Mm from the source location. Right in front of it an intensity enhancement is present. A definite identification with a stationary brightening is difficult due to its relatively weak appearance compared to the background level of 1.0. This brightening lasts for at least 40 min after the passage and is only slowly fading away. In front of this intensity enhancement a dip in the profile is propagating away from the initiation center, which we interpret as the rarefaction region, similar to the event of 2007 May 19.

5. Discussion and Conclusions

1. We analyzed four well pronounced EUV wave events observed by the STEREO EUVI telescopes in order to compare two different kinematical analysis techniques, the generally used visual tracking method and the semi-automated perturbation profiles. The differences in the determined positions of the leading edge of the wave fronts using both methods are maximal 40 Mm. Thus, we conclude that the perturbation profiles are a suitable method to analyze large-scale waves. The big advantage of the perturbation profile method is the higher degree of automatization and reproductiveness due to the objective measurements of the wave location. Nevertheless, there are some restrictions. In the later evolution phase, the wave fronts become more irregular showing changes in shapes and propagation direction. These effects are not considered in the profile method. Thus, due to the lower amplitude and the smearing of irregular fronts the wave profile is no longer distinct against the background. These properties lead to a systematic underestimation of the distance of the wave compared to the visual tracking method. Additionally, the diffuse bright fronts are easier to identify in RR images due to the fact that they have a higher contrast than BR images.

2. The determined propagation velocity derived from both methods match within the error limits. For the four wave events under study, we obtain mean velocity values in the range of $220 - 350$ km s^{-1}, i.e. within the velocity range for fast magnetosonic waves during quiet Sun conditions (e.g. Mann et al. 1999). Three of the four kinematical curves show only small deceleration values of -6 up to -13 m s^{-2}, which lie within the error range. For the fastest event of 2007 May 19, the obtained deceleration of -193 m s^{-2} is significant.

   Long et al. (2011) has analyzed the kinematics of the May 19, 2007 and February

13, 2009 events with a similar perturbation profile method. They find for the May 19, 2007 event the following values: start velocity v_0=447±87 km s^{-1}, acceleration a=–256±134 m s^{-2}, a broadening of the pulse width from 50 to 200 Mm and a decrease of the peak amplitude intensity from 60 to 15% of the background values. Our findings are v_0=429±58 km s^{-1}, a=–85±60 m s^{-2}, and similar results for the broadening of the pulse and their intensity evolution. For the second event of February 13, 2009, Long et al. (2011) find v_0=274±53 km s^{-1}, a=–49±34 m s^{-2} while our results are v_0=261±72 km s^{-1}, a=–24±30 m s^{-2}. The profile broadening and the intensity evolution is again similar. For the February 13, 2009 event the outcomes of both studies are consistent within the error limits. The results of May 19, 2007 show differences in the acceleration values which can be explained by taking into account that the method used by Long et al. (2011) and ours is not identical. 1) While they are extracting the position of maximum intensity we are using the leading edge of the wave fronts for our analysis. The difference in the acceleration values is thus due to this usage of different features for the position measurements. The maximum intensity peaks are propagating at a slower speed compared to the leading edges, an effect that is expected for a feature that is broadening during its evolution. Due to that the deceleration values are smaller for the leading edge measurements while the starting velocity values are not affected. 2) The overall sector width used in Long et al. (2011) is varying from event to event while we are using a constant angular width of 45° in each event. 3) The main direction of the calculated sector as well as the the initiation centers are not exactly the same (the uncertainty is about 20 Mm).

3. Considering the events under study as low-amplitude MHD fast-mode waves the Mach numbers and wave velocity values are proportional to each other, $M_{ms} = v/v_{ms}$. Thus, from the derived Mach number evolution (from the maximum value down to $M_{ms} \approx 1$) we expect a decrease of the propagation velocity by $\Delta v \approx 100$ km s^{-1}

(2007 May 19), ≈ 35 km s^{-1} (2009 February 13), ≈ 60 km s^{-1} (2010 January 17) and ≈ 30 km s^{-1} (2010 April 29). The velocity changes we derive from the least-square quadratic fits reveal ≈ 200 km s^{-1} (2007 May 19), ≈ 40 km s^{-1} (2009 February 13), ≈ 20 km s^{-1} (2010 January 17) and ≈ 30 km s^{-1} (2010 April 29). For the 2009 February 13 and 2010 April 29 events, the derived velocity changes are in the same order of ≈ 30 km s^{-1} as the error on the velocity determination. Hence, the weak deceleration is hidden in the measurement uncertainties. For the 2007 May 19 event the result of 200 km s^{-1} clearly exceeds the error in velocity of ≈ 70 km s^{-1}, thus the deceleration is observable and significant. According to the Mach number evolution for the 2010 January 17 event, an observable deceleration of the propagating wave is expected. The determined velocity change of ≈ 60 km s^{-1} exceeds the velocity error of 20 km s^{-1}, thus masking of the deceleration by data scatter is unlikely. Nevertheless, from the kinematical measurements obtained with the visual tracking and the perturbation profiles we do not derive a significant deceleration, as it would be expected from the peak Mach number estimated for this event.

4. Each event can be followed over a period of at least 30 minutes, during which we first observe an intensification of the wave, which is followed by a steady decrease and broadening of the wave pulses as extracted from the perturbation profiles. From this we derived useful information on the characteristics of the wave pulses, like the peak amplitude, the width, and the integral of the wave pulse. The evolution of the pulse width shows a clear broadening over time by a factor of 2–3, similar to the broadening of the FWHM values. These values are typical for large-scale waves (Warmuth et al. 2004b; Wills-Davey 2006; Warmuth 2010; Veronig et al. 2010). The integral below the perturbation profile basically remains constant (2007 May 19 and 2010 April 29) or decreases by a factor of $3-4$ (2009 February 13 and 2010 January 17). We want to stress that the combination of profile broadening and amplitude decay leading to a

constant integral below the disturbance profile is consistent with the characteristics of a freely propagating wave (Landau & Lifshitz 1987).

5. The peak magnetosonic Mach numbers derived for the events under study are in the range of $M_{\rm ms} = 1.08 - 1.21$, indicative of the evolution of weak coronal shocks. The magnetosonic Mach number for 2007 May 19 was determined via two different approaches leading to similar results in a range of $M_{\rm ms} = 1.2 - 1.4$. Thus, the usage of the perturbation maximum amplitude for the determination of the magnetosonic Mach number seems reasonable. Grechnev et al. (2011) discussed the problem of projection effects in measurements of EUV wave. Since we do not observe the perturbation from a view-point that is located directly above the propagating disturbance but from an inclined position, the intensity values are always underestimated. This is probably also the reason why we do observe Gaussian wave pulse profiles instead of a sharp edge, expected in the case of a shocked disturbance.

6. We observe three different distinct features in the perturbation profiles occurring after the wave passage. In three of four events deep coronal dimmings are prominent at small distances from the eruption center. Only for the 2010, January 17 event it is hardly present in the perturbation profiles of the used sector. However, an inspection of Figure 3 reveals the existence of coronal dimmings in the near vicinity of the initiation site most prominent to the western sectors close to the limb and also off-limb.

   The second distinct feature in the wake of three of the four the EUV waves are stationary brightenings. These stationary parts appear after the waves' passage at distances of 100–300 Mm and fade only slowly away. Due to the fact that the the most intense wave profile always forms one frame before the stationary brightening appears, these parts seem to be an obstacle for the wave front. These stationary brightenings

are not circumferential around the eruption center but confined to specific sectors, which is best observed for the event of 2009 February 13. Cohen et al. (2009) did numerical simulations on this event and showed that stationary brightenings are developing at the outer edges of the core coronal dimmings. Observations by Delannée & Aulanier (1999); Delannée (2000) and Delannée et al. (2008) as well as simulations by Chen et al. (2005) indicate that these stationary brightenings appear at the locations where the connectivity of the magnetic field lines changes. Since these stationary brightenings are located in front of the deep core dimming regions (interpreted as the footprints of the expanding CME), are restricted in their expansion (their maximal distance is given by the first wave fronts location) and appear only in confined sectors after the waves' passage, they can be interpreted as a signature of the CME expanding flanks.

The third distinct feature are rarefaction regions observable in two of four wave events, on 2007 May 19 and 2010 April 29. The rarefaction region behind the wave pulse is a prospective feature that develops trailing a large-amplitude perturbation (Landau & Lifshitz 1987). Indeed, simulations by Cohen et al. (2009) revealed regions, which are dim in intensity and propagate after the bright wave front.

The EUV wave velocities are in the range of fast magnetosonic waves in the quiet solar corona and show either a decelerating characteristics or constant velocity (within the measurement uncertainties) during propagation. The perturbation profiles reveal intensification, broadening and decay of the propagating wave pulse, while the integral evolution is either constant, or decreasing. The small Mach numbers are indicative of a weak coronal shock. Stationary brightenings formed in confined sectors at the outer edge of the core coronal dimming can be interpreted as signatures of the expanding CME flanks. The first observable wave fronts are always located right in front of them. Thus, we

conclude that the EUV wave events can be interpreted as freely propagating, weak shock fast-mode MHD waves initiated by the CME lateral expansion.

We thank the STEREO/SECCHI teams for their open data policy. N.M., I.W.K., and A.M.V. acknowledge the Austrian Science Fond (FWF): P20867-N16. The European Community's Seventh Framework Programme (FP7/2007-2013) under grant agreement no. 218816 (SOTERIA) is acknowledged by B.V. and M.T.

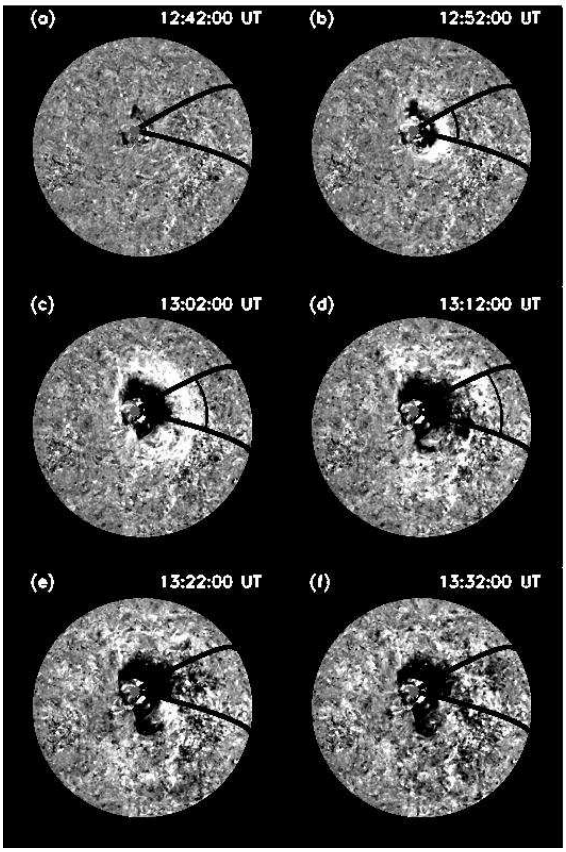

Fig. 1.— Sequence of STEREO/EUVI-A BR images of the 2007 May 19 event. The determined initiation center for the EUVI wave is indicated by the cross. The black lines indicate great circles through the wave center determining the propagation direction of $10° \pm 22.5°$, on which we focus the wave analysis. The black fronts correspond to the positions of the leading edges of the wave fronts extracted from the perturbation profiles. The field of view (FoV) is x=[$-1200''$, $+1200''$], y=[$-1200''$, $+1200''$] with the origin at the center of the Sun.

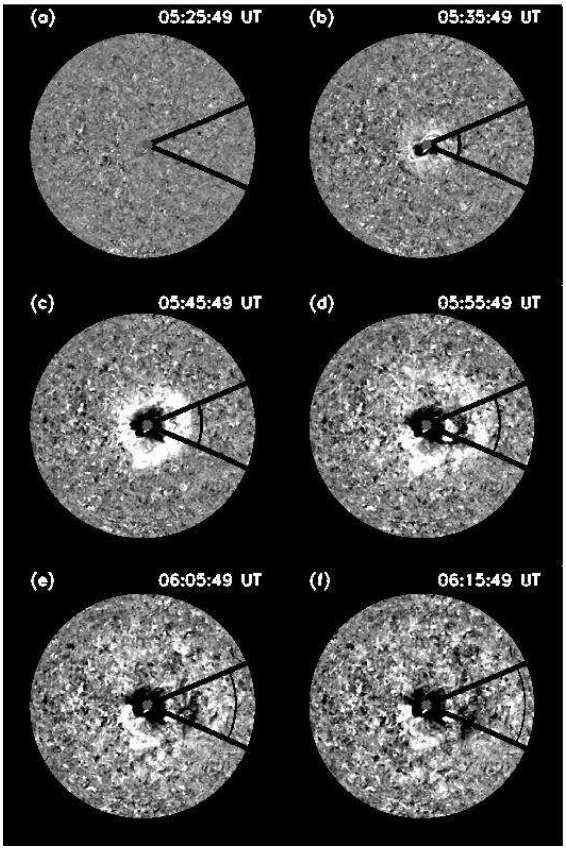

Fig. 2.— Same as Figure 1 but for the 2009 February 13 event, with the propagation direction of $340° \pm 22.5°$.

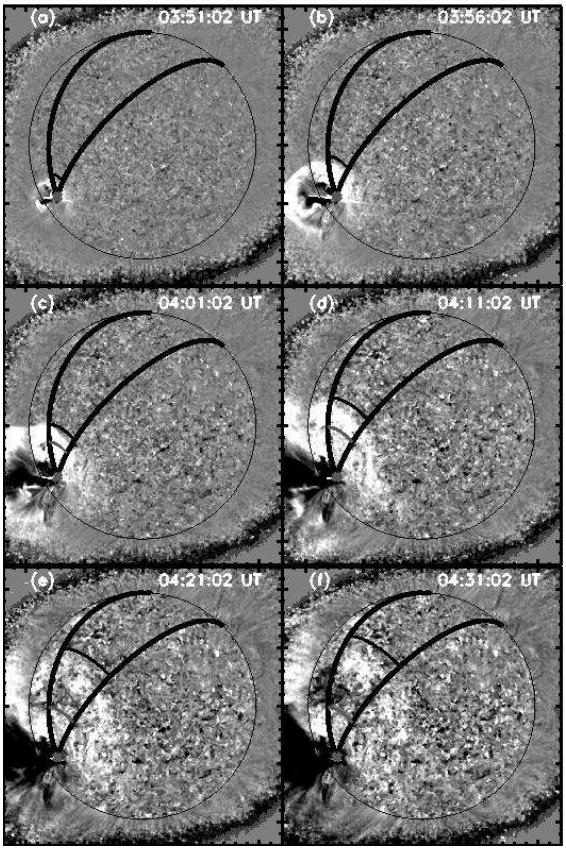

Fig. 3.— Same as Figure 3 but for the 2010 January 17 event, with the propagation direction of $65° \pm 22.5°$.

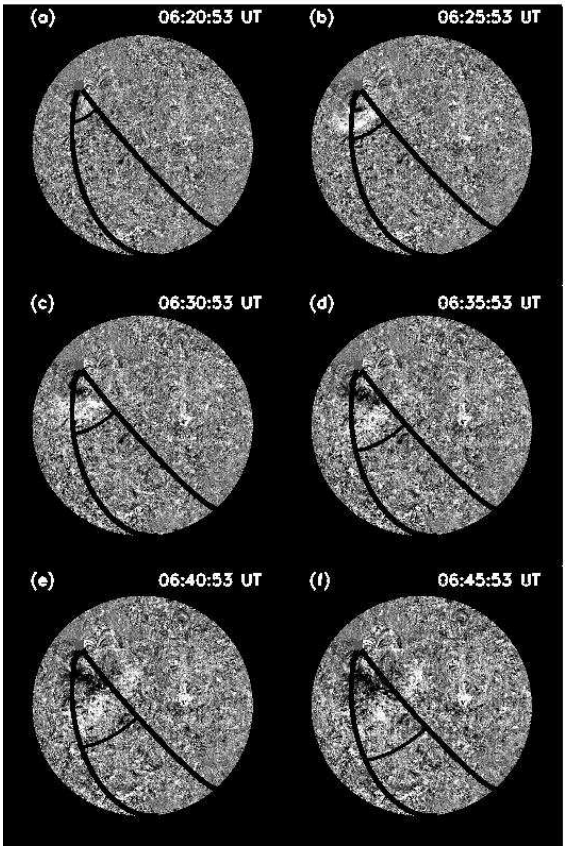

Fig. 4.— Same as Figure 4 but for the 2010 April 29 event, with the propagation direction of $300° \pm 22.5°$.

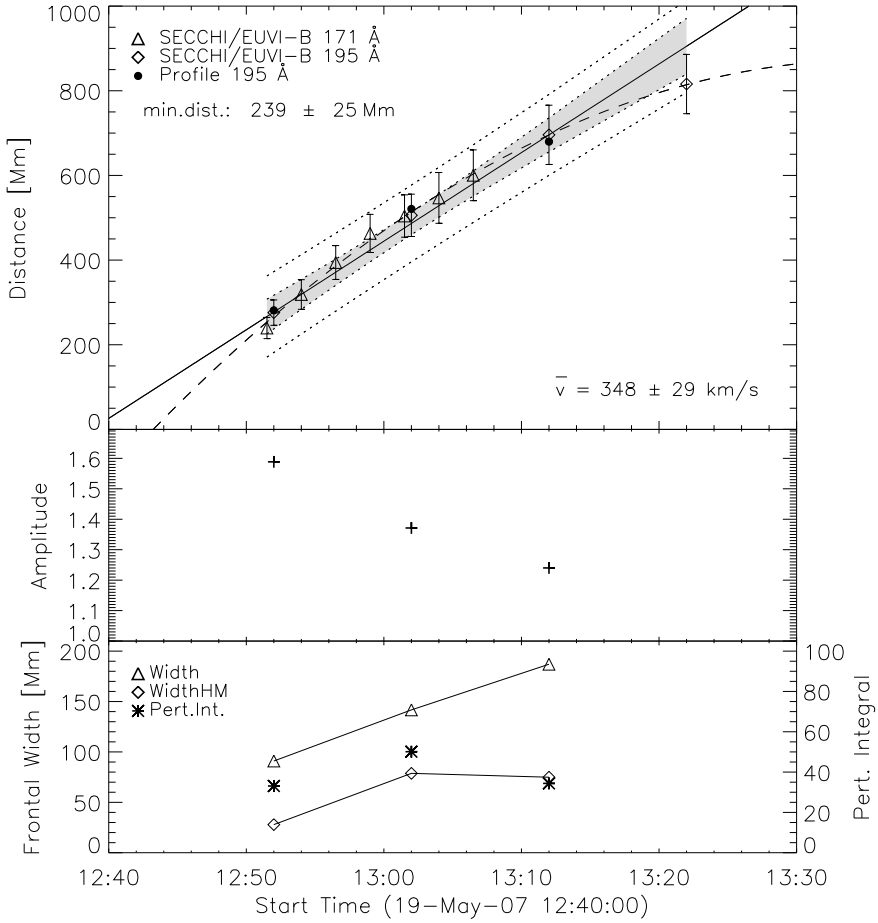

Fig. 5.— Top: Kinematics of the wave fronts of the 2007 May 19 wave observed on the solar disk in the EUVI-A 171Å (triangles) and 195Å (diamonds) channels by the visual tracking method together with the kinematical measurements we derived from the perturbation profiles (full circles). The error bars added to the measurements represent the diffusiveness of the wave fronts. The solid and dashed lines indicate the linear and quadratic least square fits to the data set obtained by visual tracking, respectively. The dotted lines indicate the 95% confidence interval (filled grey area) and the prediction boundary of the linear fit. Middle: Evolution of the amplitude of the perturbation profiles shown in Figure 9. Bottom: Evolution of the frontal width of the wave pulse (triangles), the full width at half maximum (FWHM, squares) and the integral of the gaussian envelopes (asterisks).

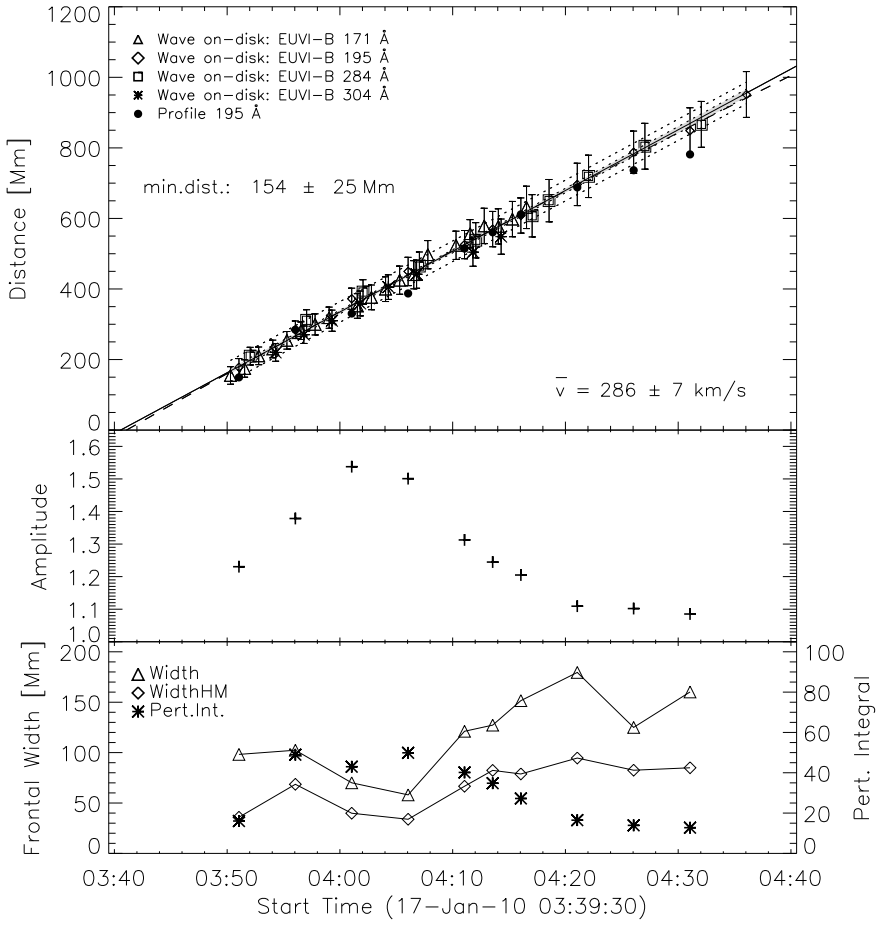

Fig. 6.— Same as in Fig. 5 but for the 2010 January 17 wave. Top: Kinematics of the wave fronts are derived from the EUVI-B 171Å (triangles), 195Å (diamonds), 284Å (squares) and 304Å (asterisks) observations.

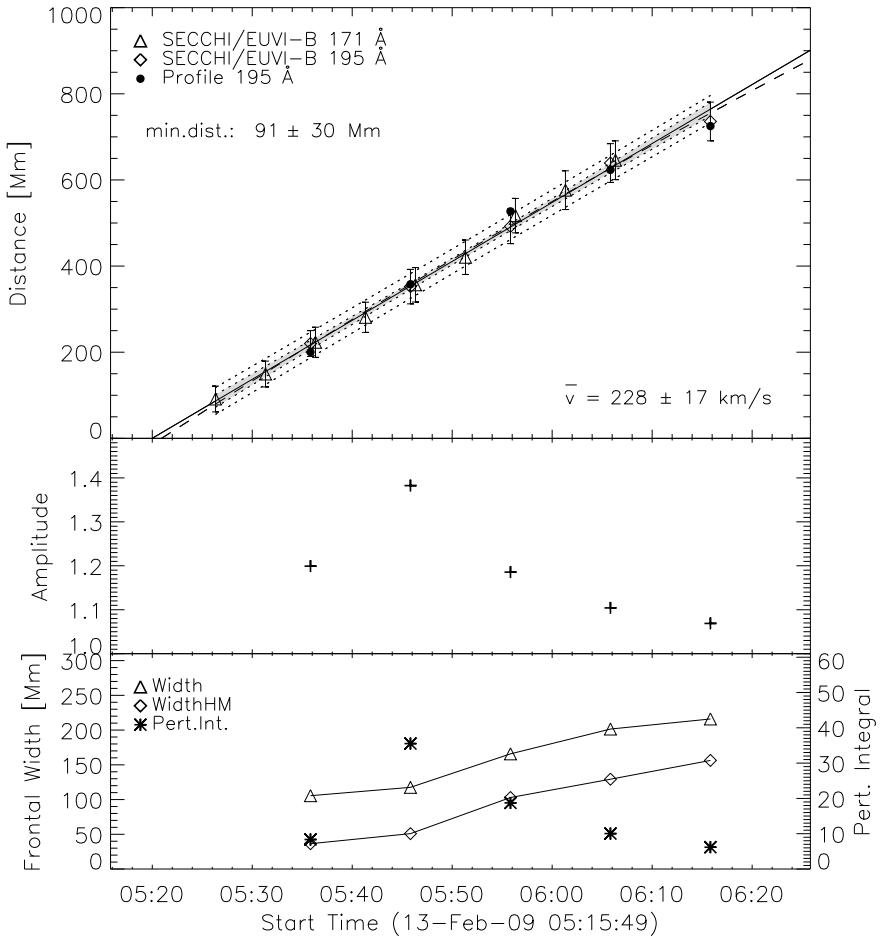

Fig. 7.— Same as in Fig. 5 but for the 2009 February 13 wave.

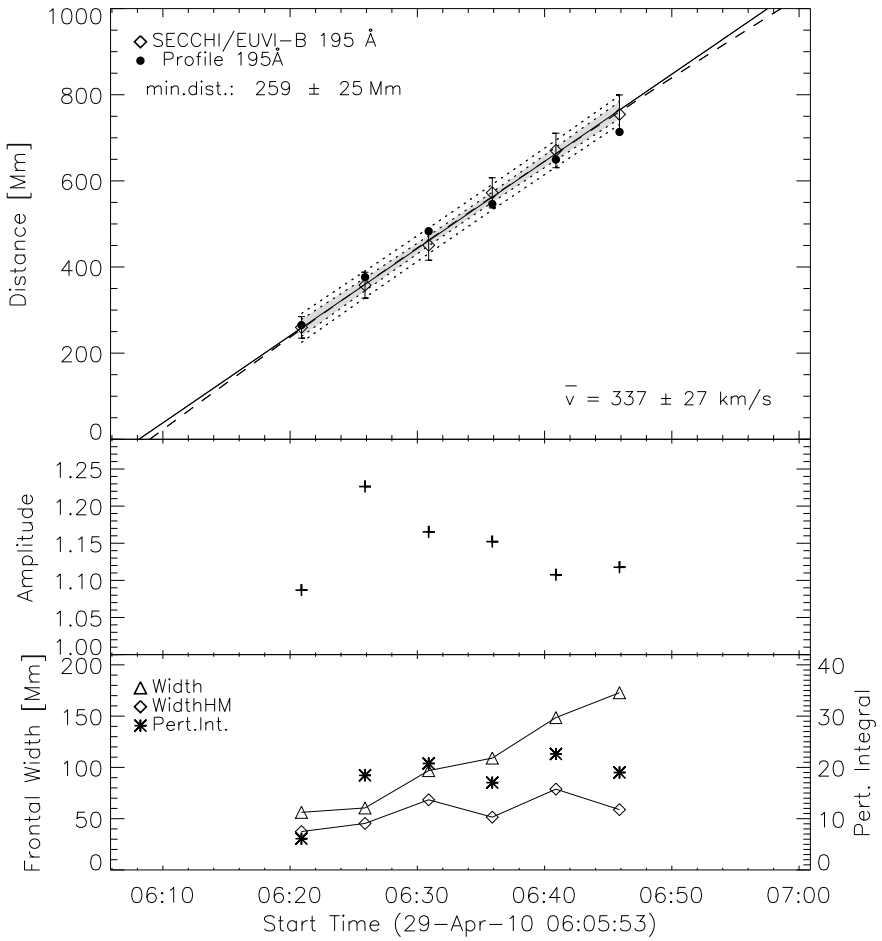

Fig. 8.— Same as in Fig. 5 but for the 2010 April 28 wave.

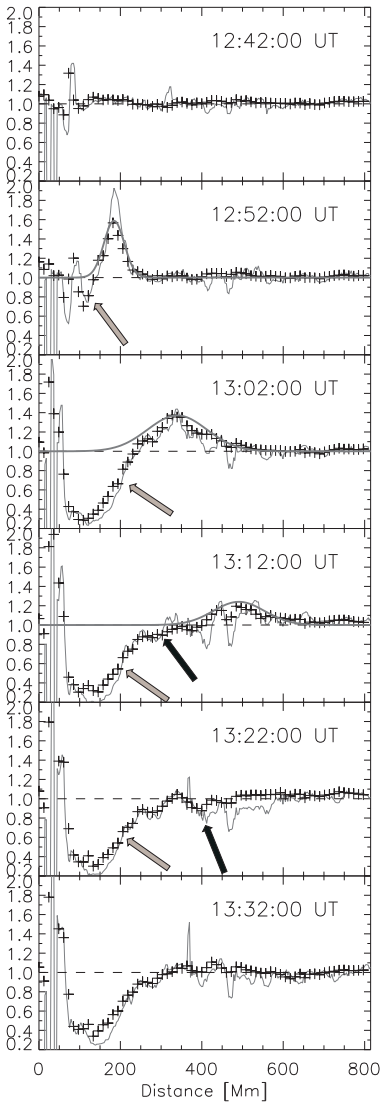

Fig. 9.— Perturbation profiles of 2007 May 19 ST-A observations in the analyzed sector ($10° \pm 22.5°$) together with the gaussian envelopes of the wave pulses (thick grey curves). The thin grey perturbation profiles correspond to the narrow sector of $8 \pm 2°$. The grey arrows point to the core dimming while the black arrows point to the rarefaction region.

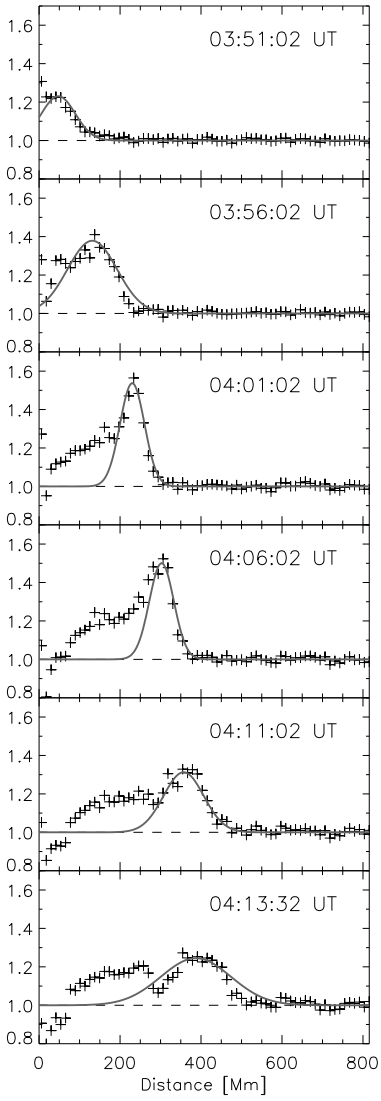

Fig. 10.— Perturbation profiles of 2010 January 17 ST-B observations in the analyzed sector ($65° \pm 22.5°$) together with the gaussian envelopes of the wave pulses (thick grey curves).

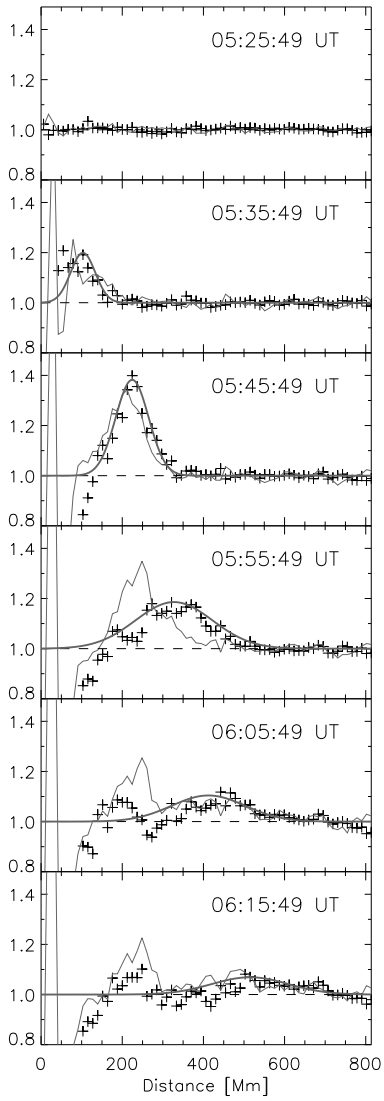

Fig. 11.— Perturbation profiles of 2009 February 13 ST-A observations in the analyzed sector ($45° \pm 22.5°$) together with the gaussian envelopes of the wave pulses (thick grey curves). The thin grey perturbation profiles correspond to the sector of $270° \pm 22.5°$.

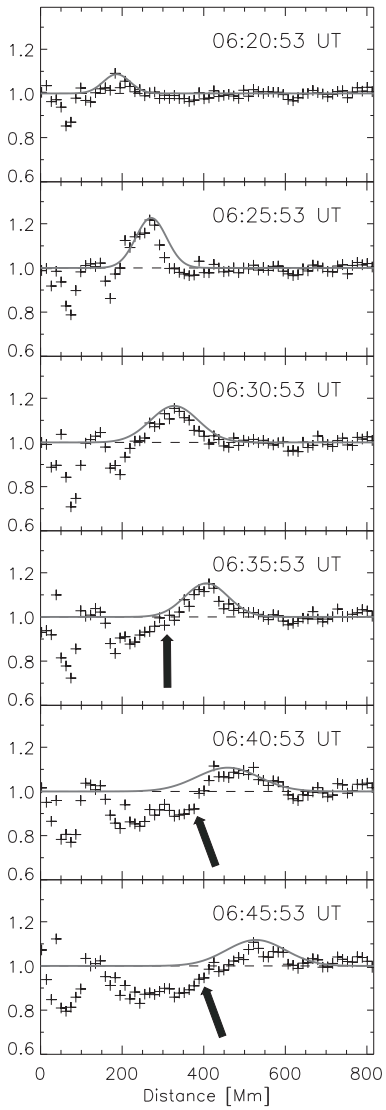

Fig. 12.— Perturbation profiles of 2010 April 29 ST-B observations in the analyzed sector ($65° \pm 22.5°$) together with the gaussian envelopes of the wave pulses (thick grey curves). The black arrows point to the rarefaction region.

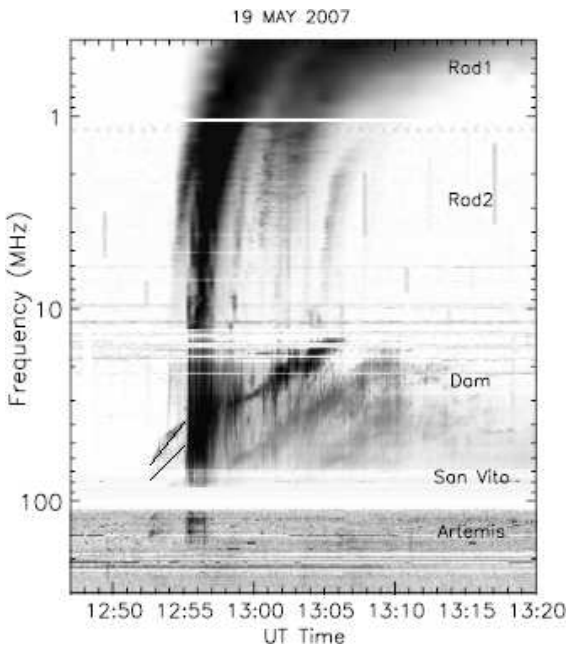

Fig. 13.— A composite dynamic radio spectrum in the frequency range 0.4 - 300 MHz (adapted from Kerdraon et al. (2010)). Type II and type III bursts are clearly visible. The two branches of the bandsplit of the fundamental emission band are marked by black lanes.

REFERENCES

Attrill, G. D. R. 2010, ApJ, 718, 494

Attrill, G. D. R., Harra, L. K., van Driel-Gesztelyi, L., & Démoulin, P. 2007, ApJ, 656, L101

Biesecker, D. A., Myers, D. C., Thompson, B. J., Hammer, D. M., & Vourlidas, A. 2002, ApJ, 569, 1009

Chen, P. F., Ding, M. D., & Fang, C. 2005, Space Science Reviews, 121, 201

Chen, P. F., Wu, S. T., Shibata, K., & Fang, C. 2002, ApJ, 572, L99

Chertok, I. M. & Grechnev, V. V. 2005, Sol. Phys., 229, 95

Cliver, E. W., Laurenza, M., Storini, M., & Thompson, B. J. 2005, ApJ, 631, 604

Cohen, O., Attrill, G. D. R., Manchester, IV, W. B., & Wills-Davey, M. J. 2009, ArXiv e-prints

Crooker, N. U. & Webb, D. F. 2006, Journal of Geophysical Research (Space Physics), 111, 8108

Del Zanna, G., Bromage, B. J. I., & Mason, H. E. 2003, A&A, 398, 743

Delaboudinière, J.-P., Artzner, G. E., Brunaud, J., et al. 1995, Sol. Phys., 162, 291

Delannée, C. 2000, ApJ, 545, 512

Delannée, C. & Aulanier, G. 1999, Sol. Phys., 190, 107

Delannée, C., Hochedez, J.-F., & Aulanier, G. 2007, A&A, 465, 603

Delannée, C., Török, T., Aulanier, G., & Hochedez, J.-F. 2008, Sol. Phys., 247, 123

Domingo, V., Fleck, B., & Poland, A. I. 1995, Sol. Phys., 162, 1

Downs, C., Roussev, I. I., van der Holst, B., et al. 2011, ApJ, 728, 2

Feldman, U., Widing, K. G., & Warren, H. P. 1999, ApJ, 522, 1133

Gallagher, P. T. & Long, D. M. 2010, ArXiv e-prints

Gopalswamy, N., Yashiro, S., Temmer, M., et al. 2009, ApJ, 691, L123

Grechnev, V. V., Afanasyev, A. N., Uralov, A. M., et al. 2011, Sol. Phys., submitted

Harra, L. K., Hara, H., Imada, S., et al. 2007, PASJ, 59, 801

Harra, L. K. & Sterling, A. C. 2001, ApJ, 561, L215

Howard, R. A., Moses, J. D., Vourlidas, A., et al. 2008, Space Science Reviews, 136, 67

Hudson, H. S., Acton, L. W., & Freeland, S. L. 1996, ApJ, 470, 629

Kaiser, M. L., Kucera, T. A., Davila, J. M., et al. 2008, Space Science Reviews, 136, 5

Kerdraon, A., Pick, M., Hoang, S., Wang, Y., & Haggerty, D. 2010, ApJ, 715, 468

Khan, J. I. & Aurass, H. 2002, A&A, 383, 1018

Kienreich, I. W., Temmer, M., & Veronig, A. M. 2009, ApJ, 703, L118

Kienreich, I. W., Veronig, A. M., Muhr, N., et al. 2011, ApJ, 727, L43+

Klassen, A., Aurass, H., Mann, G., & Thompson, B. J. 2000, A&AS, 141, 357

Landau, L. D. & Lifshitz, E. M. 1987, Fluid Mechanics, 2nd edn. (Oxford)

Long, D. M., Gallagher, P. T., McAteer, R. T. J., & Bloomfield, D. S. 2008, ApJ, 680, L81

Long, D. M., Gallagher, P. T., McAteer, R. T. J., & Bloomfield, D. S. 2011, A&A, submitted

Ma, S., Wills-Davey, M. J., Lin, J., et al. 2009, ApJ, 707, 503

Mandrini, C. H., Nakwacki, M. S., Attrill, G., et al. 2007, Sol. Phys., 244, 25

Mandrini, C. H., Pohjolainen, S., Dasso, S., et al. 2005, A&A, 434, 725

Mann, G., Klassen, A., Estel, C., & Thompson, B. J. 1999, in ESA Special Publication, Vol. 446, 8th SOHO Workshop: Plasma Dynamics and Diagnostics in the Solar Transition Region and Corona, ed. J.-C. Vial & B. Kaldeich-Schü, 477–+

Moreton, G. E. & Ramsey, H. E. 1960, PASP, 72, 357

Moses, D., Clette, F., Delaboudinière, J., et al. 1997, Sol. Phys., 175, 571

Muhr, N., Vršnak, B., Temmer, M., Veronig, A. M., & Magdalenić, J. 2010, ApJ, 708, 1639

Nelson, G. J. & Melrose, D. B. 1985, Type II bursts, ed. McLean, D. J. & Labrum, N. R., 333–359

Ofman, L. 2007, ApJ, 655, 1134

Ofman, L. & Thompson, B. J. 2002, ApJ, 574, 440

Patsourakos, S. & Vourlidas, A. 2009, ApJ, 700, L182

Patsourakos, S., Vourlidas, A., Wang, Y. M., Stenborg, G., & Thernisien, A. 2009, Sol. Phys., 90

Phillips, K. J. H., Feldman, U., & Landi, E. 2008, Ultraviolet and X-ray Spectroscopy of the Solar Atmosphere, ed. Phillips, K. J. H., Feldman, U., & Landi, E. (Cambridge University Press)

Podladchikova, O. & Berghmans, D. 2005, Sol. Phys., 228, 265

Pohjolainen, S., Maia, D., Pick, M., et al. 2001, ApJ, 556, 421

Priest, E. R. 1982, Solar magneto-hydrodynamics, 74P–+

Saito, K. 1970, Annals of the Tokyo Astronomical Observatory, 12, 53

Temmer, M., Veronig, A. M., Gopalswamy, N., & Yashiro, S. 2011, Sol. Phys.

Terradas, J. & Ofman, L. 2004, ApJ, 610, 523

Thompson, B. J., Gurman, J. B., Neupert, W. M., et al. 1999, ApJ, 517, L151

Thompson, B. J. & Myers, D. C. 2009, ApJS, 183, 225

Thompson, B. J., Plunkett, S. P., Gurman, J. B., et al. 1998, Geophys. Res. Lett., 25, 2465

Uchida, Y. 1968, Sol. Phys., 4, 30

Veronig, A. M., Muhr, N., Kienreich, I. W., Temmer, M., & Vršnak, B. 2010, ApJ, 716, L57

Veronig, A. M., Temmer, M., & Vršnak, B. 2008, ApJ, 681, L113

Veronig, A. M., Temmer, M., Vršnak, B., & Thalmann, J. K. 2006, ApJ, 647, 1466

Vršnak, B., Aurass, H., Magdalenić, J., & Gopalswamy, N. 2001, A&A, 377, 321

Vršnak, B. & Cliver, E. W. 2008, Sol. Phys., 253, 215

Vršnak, B., Warmuth, A., Brajša, R., & Hanslmeier, A. 2002, A&A, 394, 299

Vršnak, B., Warmuth, A., Temmer, M., et al. 2006, A&A, 448, 739

Wang, Y.-M. 2000, ApJ, 543, L89

Warmuth, A. 2010, Advances in Space Research, 45, 527

Warmuth, A., Vršnak, B., Aurass, H., & Hanslmeier, A. 2001, ApJ, 560, L105

Warmuth, A., Vršnak, B., Magdalenić, J., Hanslmeier, A., & Otruba, W. 2004a, A&A, 418, 1101

Warmuth, A., Vršnak, B., Magdalenić, J., Hanslmeier, A., & Otruba, W. 2004b, A&A, 418, 1117

Wills-Davey, M. J. 2006, ApJ, 645, 757

Wills-Davey, M. J. & Attrill, G. D. R. 2010, Space Science Reviews, 22

Wills-Davey, M. J., DeForest, C. E., & Stenflo, J. O. 2007, ApJ, 664, 556

Wills-Davey, M. J. & Thompson, B. J. 1999, Sol. Phys., 190, 467

Wu, S. T., Zheng, H., Wang, S., et al. 2001, J. Geophys. Res., 106, 25089

Wuelser, J., Lemen, J. R., Tarbell, T. D., et al. 2004, in Presented at the Society of Photo-Optical Instrumentation Engineers (SPIE) Conference, Vol. 5171, Society of Photo-Optical Instrumentation Engineers (SPIE) Conference Series, ed. S. Fineschi & M. A. Gummin, 111–122

Zhukov, A. N. 2011, Journal of Atmospheric and Solar-Terrestrial Physics

Zhukov, A. N. & Auchère, F. 2004, A&A, 427, 705